https://doi.org/10.20965/jrm.2023.p0328

Paper:

Autonomous Flight Using UWB-Based Positioning System with Optical Flow Sensors in a GPS-Denied Environment

Yoshiyuki Higashi* **and Kenta Yamazaki****

*Faculty of Mechanical Engineering, Kyoto Institute of Technology
Goshokaido-cho, Matsugasaki, Sakyo-ku, Kyoto, Kyoto 606-8585, Japan
E-mail: higashi@kit.ac.jp
**Division of Mechanodesign, Kyoto Institute of Technology
Goshokaido-cho, Matsugasaki, Sakyo-ku, Kyoto, Kyoto 606-8585, Japan
[Received October 7, 2022; accepted February 15, 2023]

This study presents the positioning method and autonomous flight of a quadrotor drone using ultra-wideband (UWB) communication and an optical flow sensor. UWB communication obtains the distance between multiple ground stations and a mobile station on a robot, and the position is calculated based on a multilateration method similar to global positioning system (GPS). The update rate of positioning using only UWB communication devices is slow; hence, we improved the update rate by combining the UWB and inertial measurement unit (IMU) sensor in the prior study. This study demonstrates the improvement of the positioning method and accuracy by sensor fusion of the UWB device, an IMU, and an optical flow sensor using the extended Kalman filter. The proposed method is validated by hovering and position control experiments and also realizes a sufficient rate and accuracy for autonomous flight.

Keywords: UWB, optical flow sensor, navigation, drone, sensor fusion

1. Introduction

Recently, several manufacturers have begun to manufacture and vend multirotor-style drones that are now attainable at cost-effective prices. A benefit of multirotors is that, unlike fixed-wing models, they can take off and land vertically, hover, and are easier to manipulate than single-rotor helicopters. Accordingly, in addition to tasks where aerial cinematography is central, there is an escalating necessity for multirotors in transportation and infrastructure inspection. Particularly in the realm of transportation, even amidst the worldwide coronavirus disease 2019 (COVID-19) pandemic, attempts are being made to transport straightforward packages and blood and biological samples, as drone transportation avoids direct human contact. Yakushiji et al. transported blood utilizing a quadrotor drone and demonstrated the proficiency of transporting red blood cell solutions by analyzing and comparing the outcomes before and after the flight [1]. Kunovjanek and Wankmüller proposed a drone-based emergency supply delivery system. This study deliberates the feasibility of the system by constructing a mathematical model that considers the parameters of the actual COVID-19 mobile testing team, as indicated by the time and cost involved [2].

While visual inspections of infrastructure are mainly conducted by photographing objects, there have been efforts to devise flight path planning around inspection targets [3], as well as enhance the management capabilities at construction sites by taking aerial photographs [4]. Shihavuddin et al. proposed an automatic damage-detection system that utilizes deep learning for post-inspection processing to augment the efficiency of wind-turbine inspections [5].

A drone that can adhere to H-shaped steel and inspect it while the rotor is stopping is being developed [6, 7] to increase the inspection time and diversify inspection methods. The drone is equipped with an electropermanent magnet [8], which is a magnetic adsorption device with the advantages of both permanent magnet and electromagnet. As the electropermanent magnet can control the adhesion and release modes by a pulse current, it can adsorb on steel without consuming electricity during adsorption [9]. For more efficient and safer inspections, the autonomous flight is required to fly to the inspection point. However, the lower part of the structure to be inspected, such as a bridge or other structures made of steel, is a global positioning system (GPS)-denied environment that GPS signals cannot reach. The positioning method for flying drones is key to navigation in such environments.

Motion capture systems, simultaneous localization and mapping (SLAM), and ultra-wideband (UWB) communications can be employed as positioning methods in GPS-denied environments. Motion capture can be utilized in environments enclosed in multiple cameras, and although the measurement area is not large in relation to the number of cameras installed, a highly accurate position can be obtained at update rates of 100 Hz or higher. Therefore, it is useful for verifying control algorithms and essential technologies [10]. SLAM is a positioning method employed for generating a map while moving and

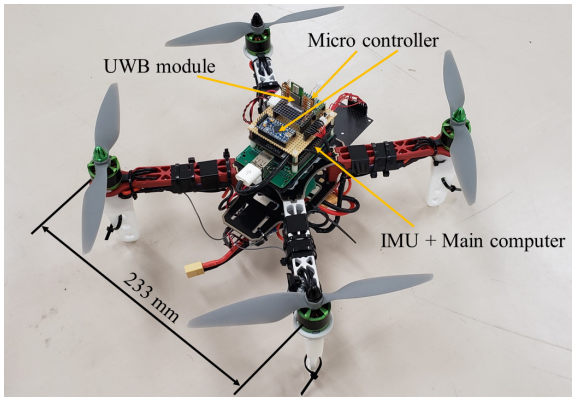

Fig. 1. Upper side of quadrotor for experiments.

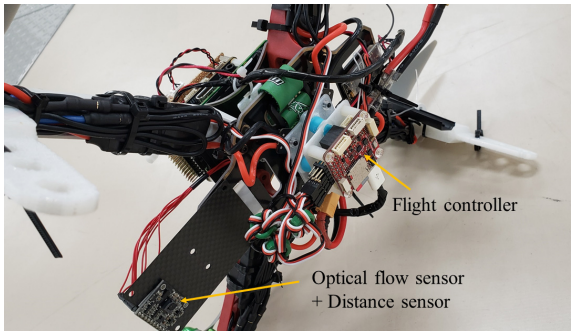

Fig. 2. Back side of quadrotor.

Table 1. Specifications of the quadrotor with the UWB communication device.

Total weight [kg]	1.05
Height [mm]	200
Width [mm]	233
Depth [mm]	233
Propeller size [inch]	8×4.5
Maximum flight time [min]	10
KV value [rpm/V]	920
Battery capacity [mAh]	2650

Table 2. Specifications of sensors.

UWB communication module (DWM1000)	
Size (W × H × D) [mm]	$13 \times 23 \times 3$
Weight [g]	1.4
Frequency range [MHz]	3244–6999
Channel bandwidth [MHz]	500
Communication range [m]	60
Optical flow sensor (PMW3901)	
Size (W × H × D) [mm]	$20 \times 26 \times 4$
Weight [g]	2.7
FOV [°]	42
Resolution [pixel]	30×30
Working range [mm]	80–2000
Measurement limit [m/s]	14.4
IMU (Navio2)	
Size (W × H × D) [mm]	$55 \times 65 \times 16$
Weight [g]	23
Accelerometer range [G]	±16
Gyroscope range [°/s]	±2000

estimating the position on the map, even in environments where no prior map information is available [11]. Because LIDAR and cameras are utilized to measure the surrounding environment, onboard devices are heavy owing to the high processing load. Suzuki realized seamless navigation of drones in GPS and GPS-denied environments by combining GPS and SLAM [12].

In UWB positioning, multiple ground stations (anchors) are pre-installed in the flight space and communication is done with a mobile station (tag) mounted on a drone using radio waves in the high-frequency spectrum of roughly 3–10 GHz to measure the inter-anchor and tag distances. This then facilitates the attainment of three-dimensional (3D) coordinates via multilateration principles akin to those employed by GPS [13]. Although anchors are required and their installation coordinates must be acquired beforehand, UWB communication has the advantage of providing high expandability of the measurement area [14] and can also measure 3D positions without the need for a map. Although UWB positioning can provide absolute coordinates, its update rate is relatively low (approximately 10 Hz), making it unsuitable for direct drone positioning control. Our prior research demonstrated that combining UWB and an inertial measurement unit (IMU) can provide positioning results at a higher update rate and autonomous control can be realized using quadrotors of the x and y positions, except for altitude control [15]. This study describes a sensor fusion algorithm that combines UWB positioning and an optical flow sensor. We demonstrate that combining an optical flow sensor, IMU, and UWB via the extended Kalman filter (EKF) can improve the position estimation accuracy and conduct autonomous flight using the proposed system.

2. Quadrotor with UWB Communication Device and Optical Flow Sensor

Figures 1 and **2** illustrate the drone with the UWB communication device. **Tables 1** and **2** present the specifications of the quadrotor and mounted sensors, and **Fig. 3** illustrates the system configuration. The quadrotor has an IMU (Navio2) for measuring angular velocity and acceleration. The optical flow sensor board comprises an optical flow sensor (PMW3901) and a distance sensor (VL53L0X). The optical flow sensor measures the movement of brightness patterns in the captured image and sends the data via SPI communication. The distance sensor measures the distance from the ground and sends the value via I2C communication. The microcontroller

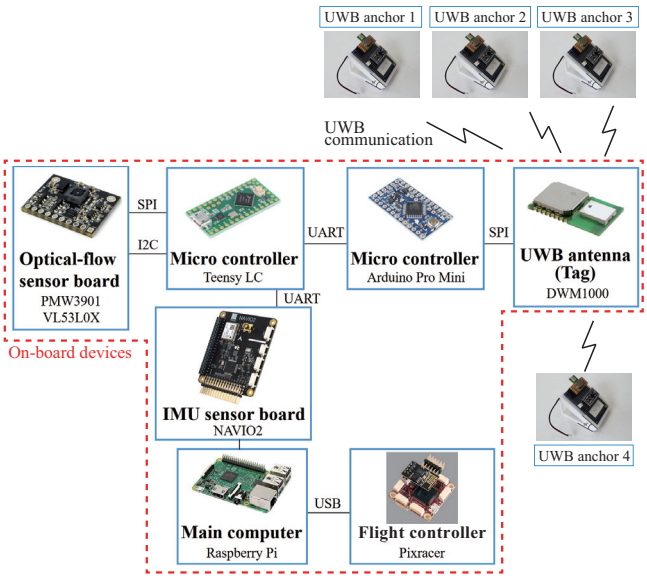

Fig. 3. System configuration of sensors.

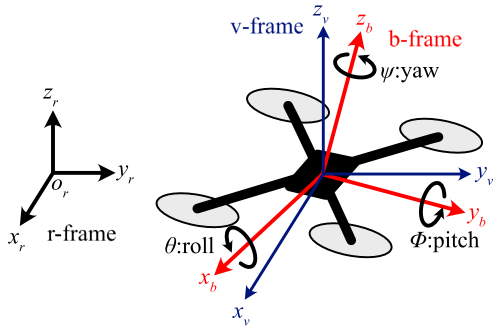

Fig. 4. Coordinate system of quadrotor.

(Teensy LC) computes the x- and y-direction velocities based on these data.

The UWB antenna (DWM1000) communicates with anchors set on the ground and obtains the distances between the quadrotor and these anchors. Positioning requires communication from a tag to at least three anchors located in the measurement field. Four anchors are utilized for positioning in this study. The microcontroller (Arduino Pro mini) receives these distances and computes the position of the quadrotor.

The main computer is a single-board computer (Raspberry Pi 4) for computation of attitude angles, position estimation, and control input to motors. The output value of the optical flow sensor changes depending on the altitude and attitude angle because it computes the velocity based on the change in pattern of the floor measured by the image sensor. Therefore, the main computer corrects the value using the altitude from the distance sensor and attitude angle. The flight controller for attitude control is the commercial device Pixracer.

Figures 4 and **5** illustrate the coordinate system of the quadrotor and the flow of the state value. The r-frame is an inertial frame fixed to the earth. The b-frame is a body

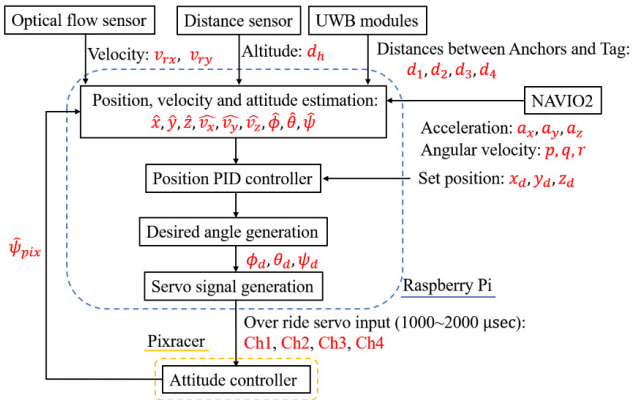

Fig. 5. Flow of the state value in the control system.

frame with its axes aligned with the sensor on the quadrotor. The axes of the v-frame are align with the r-frame, and its origin matches the origin of the b-frame. The rotation matrix [16,17] and transform of the basis vector from the v-frame to the b-frame, considering a z–y–x rotation sequence, are given by

$$\begin{bmatrix} i^b \\ j^b \\ k^b \end{bmatrix} = R_v^b(\phi,\theta,\psi) \begin{bmatrix} i^v \\ j^v \\ k^v \end{bmatrix}, \quad \ldots\ldots (1)$$

$$R_v^b(\phi,\theta,\psi) = R_{v2}^b R_{v1}^{v2} R_v^{v1}. \quad \ldots\ldots (2)$$

Here i, j, and k are unit vectors on the x-, y-, and z-axes, respectively. Superscripts b and v on the unit vectors indicate the frame. ϕ, θ, and ψ are the Euler angles around the x-, y-, and z-axes of the b-frame, respectively.

Each matrix is expressed as

$$R_v^{v1}(\psi) = \begin{bmatrix} \cos\psi(t) & \sin\psi(t) & 0 \\ -\sin\psi(t) & \cos\psi(t) & 0 \\ 0 & 0 & 1 \end{bmatrix}, \quad \ldots (3)$$

$$R_{v1}^{v2}(\theta) = \begin{bmatrix} \cos\theta(t) & 0 & -\sin\theta(t) \\ 0 & 1 & 0 \\ \sin\theta(t) & 0 & \cos\theta(t) \end{bmatrix}, \quad \ldots (4)$$

$$R_{v2}^{b}(\phi) = \begin{bmatrix} 1 & 0 & 0 \\ 0 & \cos\phi(t) & \sin\phi(t) \\ 0 & -\sin\phi(t) & \cos\phi(t) \end{bmatrix}. \quad \ldots (5)$$

The derivative of the Euler angles is expressed as follows using the angular velocity vector $\omega(t) = [p(t), q(t), r(t)]^{\mathrm{T}}$ on the b-frame:

$$\begin{bmatrix} \dot{\phi}(t) \\ \dot{\theta}(t) \\ \dot{\psi}(t) \end{bmatrix} = \begin{bmatrix} 1 & \sin\phi(t)\tan\theta(t) & \cos\phi(t)\tan\theta(t) \\ 0 & \cos\phi(t) & -\sin\phi(t) \\ 0 & \dfrac{\sin\phi(t)}{\cos\theta(t)} & \dfrac{\cos\phi(t)}{\cos\theta(t)} \end{bmatrix} \begin{bmatrix} p(t) \\ q(t) \\ r(t) \end{bmatrix}$$

$$= W(t)\omega(t). \quad \ldots\ldots (6)$$

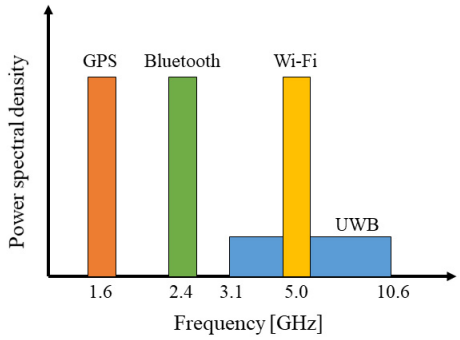

Fig. 6. Comparison of power spectrum between UWB and other wireless communication systems.

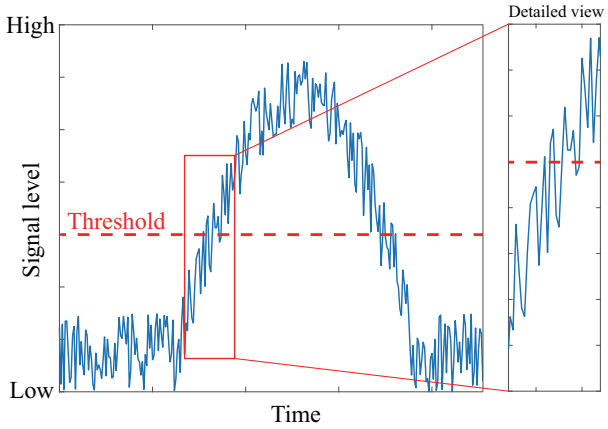

Fig. 7. Narrowband signal with noise.

3. Positioning Using UWB Communication

UWB communication is a radio communication method that uses a wider band over 500 MHz in the center frequency from 3.1 to 10.6 GHz, as shown in **Fig. 6**. The power is less than −41.3 dBm/MHz, which is lower than the noise of general electrical devices because UWB devices communicate with each other using pulses generated in the nano-second order. Nevertheless, this method results in a higher S/N ratio than narrowband communications.

Figures 7 and **8** illustrate the narrowband signal with noise and UWB signal with noise, respectively. The dashed line represents the threshold of the binary signal detected as high or low. Assuming a noiseless signal, the threshold is crossed only once when the signal changes; thus, its timing is easy to detect. However, the narrowband signal is above the threshold severally during the rise of the signal owing to noise, as indicated in the detail view. Therefore, detecting the moment when the signal changes from low to high becomes more difficult than when noise is intense. Because the UWB signal, i.e., the pulse, is easily detected whether it is above the threshold, as indicated in detail, it is immune to noise. The distance between the anchor and tag is obtained from the product of the time-of-flight (ToF) and velocity of the radio wave when the devices communicate with each other.

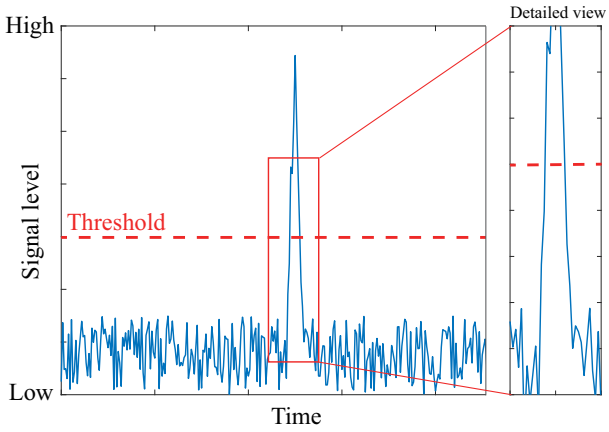

Fig. 8. Pulse by UWB signal with noise.

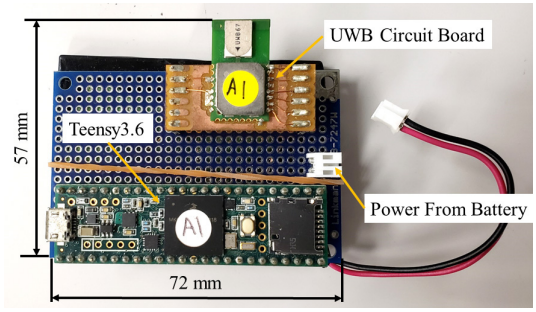

Fig. 9. UWB anchor used as ground station.

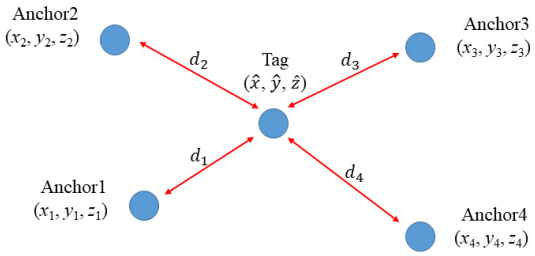

Fig. 10. Position relationship between four anchors and a tag.

The distance between UWB devices is expressed as the product of the ToF and velocity of the radio wave when the devices communicate with each other.

Figure 9 illustrates a UWB anchor comprising a chip for UWB communication (DWM1000, DecaWave Inc.), microcontroller (Teensy 3.6) for control, and Li-Po battery (1 cell, 1800 mAh). The battery can drive them for approximately 3 h.

This module communicates by transmitting radio waves from one device to another and calculates the distance between devices by multiplying the time required for communication by the speed of radio waves. It is possible to estimate the position of the robot in 3D space by the multilateration method using measured distances between devices. **Fig. 10** illustrates the relationship between the UWB tag and anchor when estimating the self-location. The multilateration method determines the posi-

tion of a tag by determining the distance between three or more fixed stations with known coordinates and the mobile station, and performing calculations based on an algorithm. This method is also employed to determine the position of a module based on the distances between multiple satellites of the global navigation satellite system (GNSS) and a GNSS mobile station. We use four anchors and one tag for positioning in this study. We utilized four anchors and one tag for positioning in this study. The positions of the anchors and tag, and the distances $d_1(t)$, $d_2(t)$, $d_3(t)$, and $d_4(t)$ between the tag and four anchors are expressed as follows:

$$\begin{bmatrix} d_1(t) \\ d_2(t) \\ d_3(t) \\ d_4(t) \end{bmatrix} = \begin{bmatrix} \sqrt{(\hat{x}(t)-x_1)^2+(\hat{y}(t)-y_1)^2+(\hat{z}(t)-z_1)^2} \\ \sqrt{(\hat{x}(t)-x_2)^2+(\hat{y}(t)-y_2)^2+(\hat{z}(t)-z_2)^2} \\ \sqrt{(\hat{x}(t)-x_3)^2+(\hat{y}(t)-y_3)^2+(\hat{z}(t)-z_3)^2} \\ \sqrt{(\hat{x}(t)-x_4)^2+(\hat{y}(t)-y_4)^2+(\hat{z}(t)-z_4)^2} \end{bmatrix}. \quad (7)$$

There are many methods to compute the position, and detailed solutions are provided in research on multilateration [18, 19]. This formula constitutes a part of the observation equation of the EKF.

4. Sensor Fusion to Positioning

This section describes a method for position estimation of the quadrotor using the EKF. The attitude angle is calculated by adopting the integral of the gyro sensor's value on the Kalman filter's state equation and converting it into the angle. However, the estimated angle drifts over time because noise on the gyro also accumulates. In addition, an attitude angle other than the yaw angle can be calculated from the value obtained from the acceleration sensor in the observation equation. At this point, the computed value did not drift. However, when the quadrotor moves in translation, extra acceleration is applied, making it impossible to calculate an accurate angle. Attitude angle estimation using the EKF effectively compensates for the disadvantages of these two types of sensors.

The position is calculated using the moving distance obtained by integrating the value of the acceleration sensor twice and distance obtained by UWB communication. Because the accelerometer can measure the acceleration at several thousand Hz, the position estimation value is also highly responsive to changes. However, the value drifts because of integration, as with the attitude angle. In addition, the estimated value using the UWB can obtain absolute coordinates without drift; however, the update frequency when using the four UWB anchors is as slow as 10 Hz. Thus, the estimated value is unsuitable for controlling the quadrotor moving at high speed. The Kalman filter is also effective in position estimation because it can compensate for the disadvantages of each sensor.

Here, we derive an algorithm for position and orientation estimation using the EKF [17]. First, the state equations are derived. The relationship between the velocity $V_r(t) = [v_x(t), v_y(t), v_z(t)]^{\mathrm{T}}$ and the position vector $P_r(t) = [x_r(t), y_r(t), z_r(t)]^{\mathrm{T}}$ can be expressed as follows:

$$\frac{d}{dt}P_r(t) = V_r(t). \quad (8)$$

The time derivative $\frac{d}{dt}V_r(t)$ of the velocity vector is expressed by the following equation using the sensor value $a_b(t) = [a_x(t), a_y(t), a_z(t)]^{\mathrm{T}}$ obtained from the acceleration sensor and rotation matrix R.

$$\frac{d}{dt}V_r(t) = Ra_b(t) - g_r. \quad (9)$$

Here, g_r is the gravity vector determined as $g_r = [0, 0, -g]^{\mathrm{T}}$ using the gravitational acceleration g. The gravity vector g_r strictly includes the acceleration in each axis caused by the motion. However, the vector comprises only gravitational acceleration, assuming that the acceleration in flight is sufficiently negligible compared to gravitational acceleration.

The relationship between the Euler angle $\Theta(t) = [\phi(t), \theta(t), \psi(t)]^{\mathrm{T}}$ and angular velocity vector $\omega(t) = [p(t), q(t), r(t)]^{\mathrm{T}}$ in the body frame is expressed as Eq. (6).

Defining the state vector as $x(t) = [\Theta(t), P_r(t), V_r(t)]^{\mathrm{T}}$, Eqs. (8) and (9) can be summarized as follows:

$$\dot{x}(t) = f(x(t)). \quad (10)$$

Here, $f(\cdot)$ is the following equation:

$$f(x(t)) = \begin{bmatrix} W(t)\omega(t) \\ V_r(t) \\ Ra_b(t) - g_r \end{bmatrix}. \quad (11)$$

However, if the noises $\delta\omega(t) = [\delta p(t), \delta q(t), \delta r(t)]^{\mathrm{T}}$ and $\delta a_b(t) = [\delta a_x(t), \delta a_y(t), \delta a_z(t)]^{\mathrm{T}}$ included in the values obtained from the gyro and acceleration sensors are considered, Eq. (10) becomes the following equation:

$$\dot{x}(t) = f(x(t)) + Bw_p(t). \quad (12)$$

B and $w_p(t)$ in the above are

$$B = \begin{bmatrix} 0_{3\times3} & 0_{3\times3} & I_{3\times3} \\ I_{3\times3} & 0_{3\times3} & I_{3\times3} \end{bmatrix}^{\mathrm{T}}, \quad (13)$$

$$w_p(t) = [\delta p(t), \delta q(t), \delta r(t), \delta a_x(t), \delta a_y(t), \delta a_z(t)]^{\mathrm{T}}. \quad (14)$$

Furthermore, discretizing Eq. (12) using Euler's method yields the following equation:

$$x[k+1] = f_t(x[k]) + B_t w_p[k]. \quad (15)$$

Here,

$$f_t(x[k]) = x[k] + f(x[k])\Delta t, \quad B_t = B\Delta t, \quad (16)$$

where Δt is the sampling period.

Furthermore, we derive the observation equation. The observed values are the distance data from the UWB module, acceleration and angular velocity from the IMU, altitude from the distance sensor, translational velocity from

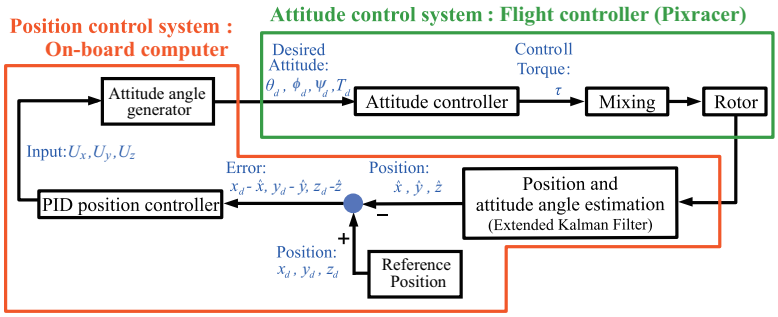

Fig. 11. Block diagram of position control system.

the optical flow sensor, and estimated yaw angle from the Pixracer, the flight controller. First, the angle is calculated using the acceleration sensor values. The relationship between the sensor value a_b obtained from the acceleration sensor and gravity vector g_r using the rotation matrix R is expressed as

$$\begin{bmatrix} a_x[k] \\ a_y[k] \\ a_z[k] \end{bmatrix} = R[k]g_r = \begin{bmatrix} g\sin\theta[k] \\ -g\cos\theta[k]\sin\phi[k] \\ -g\cos\theta[k]\cos\phi[k] \end{bmatrix}. \quad . \quad (17)$$

In Eq. (17), the yaw angle component ψ does not appear, indicating that the yaw angle cannot be estimated using only the information obtained from the acceleration sensor. Therefore, we adopt the yaw angle $\psi_{pix}[k]$ obtained from Pixracer.

Let the observation matrix be $y[k] = [a_x[k], a_y[k], a_z[k], d_1[k], d_2[k], d_3[k], d_4[k], d_h[k], \psi_{pix}[k], v_x[k], v_y[k]]^{\mathrm{T}}$; then, it is represented using Eqs. (7) and (17) and the velocities $v_x[k]$ and $v_y[k]$ obtained from the optical flow sensor.

$$y(t) = h_t(x[k]), \quad . \quad . \quad . \quad . \quad . \quad . \quad . \quad . \quad . \quad . \quad (18)$$

$$h_t(x[k]) = \begin{bmatrix} g\sin\theta[k] \\ -g\cos\theta[k]\sin\phi[k] \\ -g\cos\theta[k]\cos\phi[k] \\ d_1[k] \\ d_2[k] \\ d_3[k] \\ d_4[k] \\ d_h[k] \\ \psi_{pix}[k] \\ v_x[k] \\ v_y[k] \end{bmatrix}, \quad . \quad . \quad . \quad . \quad . \quad (19)$$

where $d_h[k]$ and $\psi_{pix}[k]$ in $y[k]$ are the distances to the ground obtained from the distance sensor and yaw angle value estimated by the Pixracer, respectively.

If we consider noises $[\delta a_x[k], \delta a_y[k], \delta a_z[k]]^{\mathrm{T}}$, $[\delta d_1[k], \delta d_2[k], \delta d_3[k], \delta d_4[k]]^{\mathrm{T}}$, $\delta d_h[k]$, $\delta\psi_{pix}[k]$, and $[\delta v_x[k], \delta v_y[k]]^{\mathrm{T}}$ included in the outputs from the accelerometer, UWB module, distance sensor, Pixracer, and optical flow sensor in Eq. (19), the observation equation becomes

$$y[k] = h_t(x[k]) + w_o[k], \quad . \quad . \quad . \quad . \quad . \quad . \quad . \quad . \quad . \quad (20)$$

where the observation noise $w_o[k]$ is

$$w_o[k] = [\delta a_x[k], \delta a_y[k], \delta a_z[k], \delta d_1[k], \delta d_2[k], \delta d_3[k], \delta d_4[k], \delta d_h[k], \delta\psi_{pix}[k], \delta v_x[k], \delta v_y[k]]^{\mathrm{T}}. \quad (21)$$

We obtain the position estimation algorithm by applying the extended Kalman filter to this discrete process model.

5. Position Controller

A block diagram of the position control system is illustrated in **Fig. 11**. In position-holding control at a fixed point, the position of the quadrotor is controlled based on the deviation between the target and estimated position. Based on the deviation between the estimated and target coordinates, the virtual input to obtain the desired angle is given as follows [20]:

$$U_x[k] = k_{px}(x_d[k] - \hat{x}) + k_{dx}(\dot{x}_d[k] - \hat{\dot{x}}) + k_{ix}\sum_{n=1}^{k}(x_d[n] - \hat{x})\Delta t, \quad . \quad . \quad . \quad . \quad . \quad . \quad (22)$$

$$U_y[k] = k_{py}(y_d[k] - \hat{y}) + k_{dy}(\dot{y}_d[k] - \hat{\dot{y}}) + k_{iy}\sum_{n=1}^{k}(y_d[n] - \hat{y})\Delta t, \quad . \quad . \quad . \quad . \quad . \quad . \quad (23)$$

$$U_z[k] = k_{pz}(z_d[k] - \hat{z}) + k_{dz}(\dot{z}_d[k] - \hat{\dot{z}}) + k_{iz}\sum_{n=1}^{k}(z_d[n] - \hat{z})\Delta t, \quad . \quad . \quad . \quad . \quad . \quad . \quad (24)$$

where the x-, y-, and z-axes are the axes in the global frame. As can be observed from the above equations, the values of the virtual inputs can be computed by a controller using the deviation. Using these input values, the target values of the pitch and roll angles can be calculated by the following equations:

$$\phi_d[k] = \frac{1}{g}(U_x[k]\sin\psi[k] - U_y[k]\cos\psi[k]), \quad . \quad (25)$$

$$\theta_d[k] = \frac{1}{g}(U_x[k]\cos\psi[k] + U_y[k]\sin\psi[k]). \quad . \quad (26)$$

These obtained values are converted into PWM signals that can be received by the flight controller, and then sent to the controller to control the rotation of each rotor. The reference yaw angle ψ_d is zero, which is the direction in which the nose of the quadrotor is facing at the beginning.

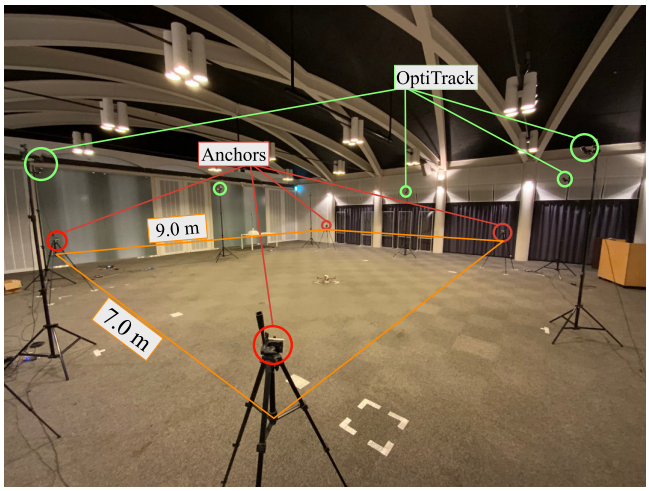

Fig. 12. Experimental environment.

Table 3. Specification of the motion capture system for experiments.

Number of cameras	6
Measurement range	9 m
Measurement frequency	100 Hz
Measurement accuracy	0.1 mm
Marker size	14 mm, sphere

It is controlled by a simple PID controller to prevent the nose from rotating in the deviation from the estimated current angle.

6. Experiments

To verify the developed control algorithm, a hovering experiment to hold the position and a position control experiment to move to the three reference points were conducted. **Fig. 12** shows the experimental environment surrounded by a motion capture system (OptiTrack). The motion capture system measures the position of IR markers shaped 14 mm sphere attached to the quadrotor by capturing images with multiple IR cameras (Flex 13). **Table 3** presents the specifications of the motion capture system. These cameras are utilized only to measure the 3D actual position at 100 Hz, not for position feedback. All experiments in this study were performed using automatic control from takeoff to landing.

Four UWB anchors were set in each corner of the measurement area. **Table 4** presents the located anchor positions.

6.1. Hovering Control

The experimental results of hovering are shown in **Figs. 13** and **14**. The drone maintained its position near the reference during the flight; however, it moved to the upper right of the graph during landing.

Compared to the results obtained by the motion cap-

Table 4. Absolute coordinates of located UWB anchors in experiments.

	x [m]	y [m]	z [m]
Anchor 1	−4.50	3.50	1.27
Anchor 2	4.50	3.50	1.27
Anchor 3	4.50	−3.50	1.27
Anchor 4	−4.50	−3.50	1.27

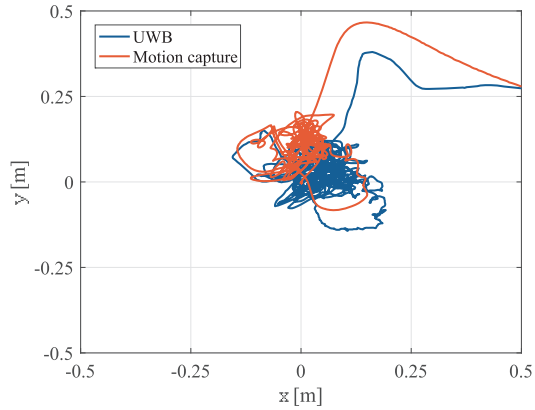

Fig. 13. Result of static position hold experiment. Reference point is origin.

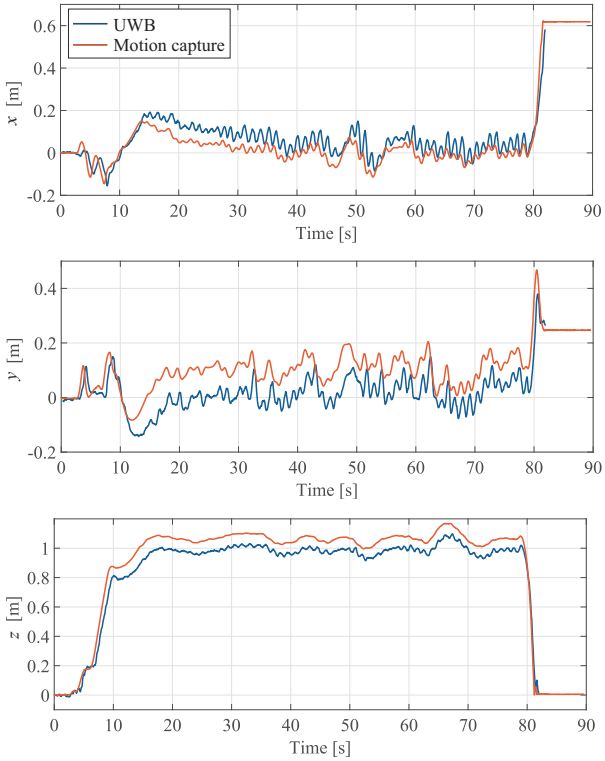

Fig. 14. Result of x, y, and z positions of the static position hold experiment.

Table 5. Comparison of measurement accuracy of the system with and without optical flow sensor.

Optical flow sensor	Mean error [m]	Variance [m^2]
With	0.1292	0.00682
Without	0.1943	0.00582

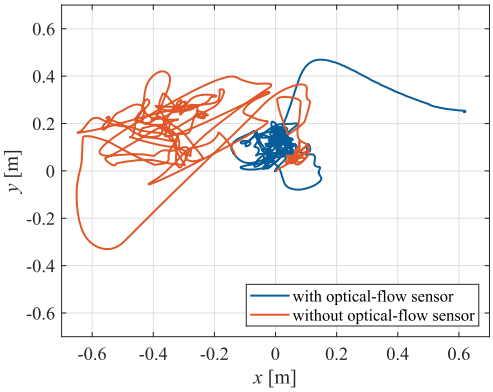

Fig. 15. Comparison of position hold control results with and without the optical flow sensor.

ture, the estimated values have an offset of approximately 0.05–0.1 m on each axis. However, the fluctuation of the values is also negligible, indicating that the optical flow sensor can hover at a constant altitude near the origin.

The mean errors e_x, e_y, and e_z of each axis between the measured value obtained from the motion capture and estimated value on the drone were $e_x = 0.0578$, $e_y = 0.0872$, and $e_z = 0.0892$. The variances were $s_x = 0.0035$, $s_y = 0.0032$, and $s_z = 0.0070$, indicating that a high position estimation accuracy can be achieved.

Here, we compare the positioning accuracy measured by the proposed system with the optical flow sensor and one without the sensor in a previous study [15]. **Table 5** presents the mean error and variance of the positioning results of both positioning systems. The mean error of the proposed method is approximately 34% lower than that of the previous system, and it is indicated that the positioning accuracy is improved by introducing the optical flow sensor.

Figure 15 shows the experimental results of position control using the algorithm with and without the optical flow sensor. Both results were measured using a motion capture system. Although the quadrotor was off the origin after takeoff, both algorithms succeeded in hovering to hold the position. The mean error from the origin and variance during hover are presented in **Table 6**. In the control without the optical flow sensor, the quadrotor hovered around $(-0.4, 0.2)$ and the mean error was higher than that with the optical flow sensor. Because the variance in the case with the optical flow sensor was also lower than that in the case without the sensor, the effectiveness of the sensor fusion with the optical flow sensor was demonstrated by the results.

Table 6. Comparison of control accuracy of the position holding experiment.

Optical flow sensor	Mean error [m]	Variance [m^2]
With	0.0959	0.00507
Without	0.3453	0.02191

Table 7. Reference way points in the navigation experiment.

	x [m]	y [m]	z [m]
Point 1	0	0	1.0
Point 2	-1.5	1.0	1.0
Point 3	1.5	-1.0	1.0

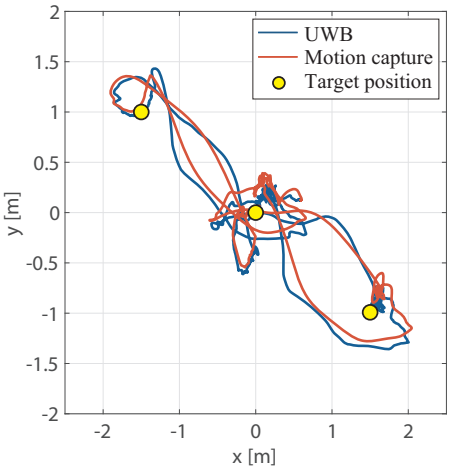

Fig. 16. Result of the position control experiment. Three dots are target points.

6.2. Position Control

Furthermore, we conducted a navigation experiment to pass through waypoints. **Table 7** presents the three reference points. The drone took off at point 1 and then moved to points 2, 1, 3, and 1 in sequence. After returning to point 1, the drone landed automatically. The experimental results are shown in **Figs. 16** and **17**.

Although an overshoot occurred near the point when moving to each target point, the drone converged to the target point, indicating that the position control was functioning. The altitude did not fluctuate significantly during movement, indicating that altitude control was also effective. The difference between the values for each axis and those obtained from the motion capture was larger than that in the hovering experiment. The mean errors e_x, e_y, and e_z of each axis between the measured value obtained from OptiTrack and estimated value from UWB were $e_x = 0.1159$, $e_y = 0.1219$, and $e_z = 0.0848$. The variances were $s_x = 0.0552$, $s_y = 0.0237$, and $s_z = 0.0058$.

Accordingly, we were able to achieve autonomous control including altitude control, which had not been achieved in a previous study [15].

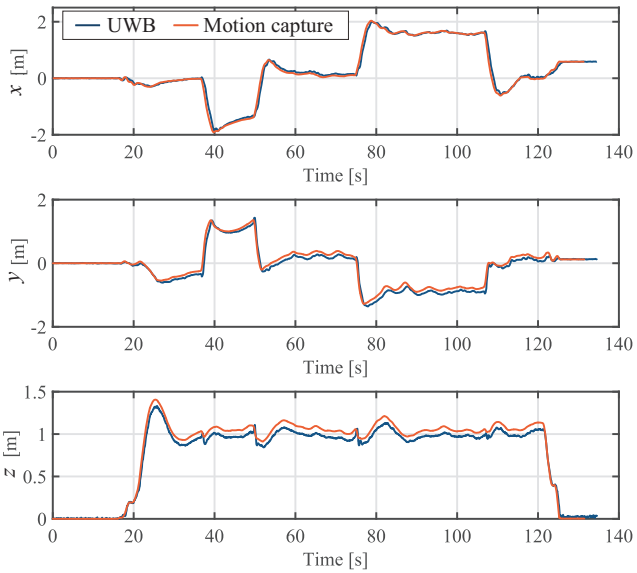

Fig. 17. x, y, and z positions of the position control experiment.

7. Conclusions

This study presented a positioning system and autonomous flight for a drone flying in GPS-denied environments such as indoors. The sensor system of the drone comprised a sensor board mounted with a gyro and accelerometer, UWB antenna to receive the positioning radio, distance sensor for measuring the altitude, and optical flow sensor to detect the motion of surfaces.

We proposed an algorithm to estimate the drone's position by integrating the output values of the IMU, UWB, optical flow sensor, and altitude sensor using the EKF. After the controller was designed as a PID controller for position control based on the estimated position, experiments were conducted to validate the accuracy of the position estimation and position control. The positioning experiment demonstrated that the proposed system could estimate with higher accuracy than the prior method without the optical flow sensor. The position-holding experiments using the proposed method indicated that the average error was less than 0.1 m. The average error and its variance were lower than those of the systems in previous studies, indicating improved position control performance. In addition, we conducted an autonomous flight experiment to move the three given points in order. The quadrotor reached the target points without significantly straying from the route while moving between points by autonomous control. The results indicated that the system combining the UWB and optical flow sensor could realize position control with high accuracy.

Acknowledgments

This work was supported by JSPS KAKENHI Grant Number JP20K04379.

References:

[1] F. Yakushiji, K. Yakushiji, M. Murata, N. Hiroi, K. Takeda, and H. Fujita, "The quality of blood is not affected by drone transport: An evidential study of the unmanned aerial vehicle conveyance of transfusion material in Japan," Drones, Vol.4, No.1, Article No.4, 2020.

[2] M. Kunovjanek and C. Wankmüller, "Containing the COVID-19 pandemic with drones – Feasibility of a drone enabled back-up transport system," Transport Policy, Vol.106, pp. 141-152, 2021.

[3] L. Shi, G. Mehrooz, and R. H. Jacobsen, "Inspection path planning for aerial vehicles via sampling-based sequential optimization," 2021 Int. Conf. on Unmanned Aircraft Systems (ICUAS), pp. 679-687, 2021. https://doi.org/10.1109/ICUAS51884.2021.9476784

[4] R. Ashour, T. Taha, F. Mohamed, E. Hableel, Y. A. Kheil, M. Elsalamouny, M. Kadadha, K. Rangan, J. Dias, L. Seneviratne, and G. Cai, "Site inspection drone: A solution for inspecting and regulating construction sites," 2016 IEEE 59th Int. Midwest Symp. on Circuits and Systems (MWSCAS), pp. 1-4, 2016. https://doi.org/10.1109/MWSCAS.2016.7870116

[5] A. Shihavuddin, X. Chen, V. Fedorov, A. N. Christensen, N. A. B. Riis, K. Branner, A. B. Dahl, and R. R. Paulsen, "Wind turbine surface damage detection by deep learning aided drone inspection analysis," Energies, Vol.12, No.4, Article No.676, 2019.

[6] S. Akahori, Y. Higashi, and A. Masuda, "Development of an aerial inspection robot with EPM and camera arm for steel structures," 2016 IEEE Region 10 Conf. (TENCON), pp. 3542-3545, 2016.

[7] K. Takeuchi, A. Masuda, S. Akahori, Y. Higashi, and N. Miura, "A close inspection and vibration sensing aerial robot for steel structures with an EPM-based landing device," Nondestructive Characterization and Monitoring of Advanced Materials, Aerospace, and Civil Infrastructure 2017, Article No.101692U, 2017.

[8] A. Masuda, A. Tanaka, Y. Higashi, and N. Miura, "Reliable activation of an EPM-based clinging device for aerial inspection robots," J. Robot. Mechatron., Vol.31, No.6, pp. 827-836, 2019.

[9] Y. Higashi, K. Yamazaki, A. Masuda, N. Miura, and Y. Sawada, "Attractive force estimation of a magnetic adsorption unit for inspection UAVs," J. Robot. Mechatron., Vol.33, No.6, pp. 1349-1358, 2021.

[10] M. W. Mueller and R. D'Andrea, "Stability and control of a quadrocopter despite the complete loss of one, two, or three propellers," 2014 IEEE Int. Conf. on Robotics and Automation (ICRA), pp. 45-52, 2014.

[11] P. Araújo, R. Miranda, D. Carmo, R. Alves, and L. Oliveira, "Air-SSLAM: A visual stereo indoor SLAM for aerial quadrotors," IEEE Geoscience and Remote Sensing Letters, Vol.14, No.9, pp. 1643-1647, 2017.

[12] S. Suzuki, "Integrated navigation for autonomous drone in GPS and GPS-denied environments," J. Robot. Mechatron., Vol.30, No.3, pp. 373-379, 2018.

[13] S. Akahori, Y. Higashi, and A. Masuda, "Position estimation system with UWB, IMU and a distance sensor for quad-rotors," 2017 IEEE Region 10 Conf. (TENCON 2017), pp. 1992-1996, 2017.

[14] Y. Yasukawa, Y. Higashi, A. Masuda, and N. Miura, "Automatic anchor calibration for UWB-based indoor positioning systems," 2020 IEEE Region 10 Conf. (TENCON), pp. 1374-1379, 2020.

[15] S. Nakamura, Y. Higashi, A. Masuda, and N. Miura, "A positioning system and position control system of a quad-rotor applying Kalman filter to an UWB module and an IMU," 2020 IEEE/SICE Int. Symp. on System Integration (SII), pp. 747-752, 2020.

[16] D. M. Henderson, "Euler angles, quaternions, and transformation matrices for space shuttle analysis," NASA Design Note No.1.4-8-020, NASA-CR-151435, 1977.

[17] K. Nonami, "Introduction to drone engineering – Modeling and control –," Corona Publishing Co., Ltd., pp. 18-35, 2020 (in Japanese).

[18] D. E. Manolakis, "Efficient solution and performance analysis of 3-D position estimation by trilateration," IEEE Trans. on Aerospace and Electronic Systems, Vol.32, No.4, pp. 1239-1248, 1996.

[19] F. Thomas and L. Ros, "Revisiting trilateration for robot localization," IEEE Trans. on Robotics, Vol.21, No.1, pp. 93-101, 2005.

[20] Z. Zuo, "Quadrotor trajecotry tracking control: A PD control algorithm," 3rd Int. Conf. on Computer and Electrical Engineering (ICCEE 2010), 2010.

Name:
Yoshiyuki Higashi

ORCID:
0000-0002-8400-8610

Affiliation:
Assistant Professor, Faculty of Mechanical Engineering, Kyoto Institute of Technology

Address:
Goshokaido-cho, Matsugasaki, Sakyo-ku, Kyoto, Kyoto 606-8585, Japan

Brief Biographical History:
2010- Assistant Professor, Kyoto Institute of Technology

Main Works:
• "Attractive force estimation of a magnetic adsorption unit for inspection UAVs," J. Robot. Mechatron., Vol.33, No.6, pp. 1349-1358, 2021.
• "Attitude control simulation of a legged aerial vehicle using the leg motions," Advances in Science, Technology and Engineering Systems J., Vol.3, No.6, pp. 204-212, 2018.

Membership in Academic Societies:
• Institute of Electrical and Electronics Engineers (IEEE)
•The Robotics Society of Japan (RSJ)
•The Japan Society of Mechanical Engineers (JSME)

Name:
Kenta Yamazaki

Affiliation:
Division of Mechanodesign, Kyoto Institute of Technology

Address:
Goshokaido-cho, Matsugasaki, Sakyo-ku, Kyoto, Kyoto 606-8585, Japan

Brief Biographical History:
2020 Received B.S. degree in Engineering from Kyoto Institute of Technology
2020- Master Course Student, Division of Mechanodesign, Kyoto Institute of Technology

Main Works:
• "Improvement of adsorption force of an EPM-based adsorb device by a suspension," 2020 IEEE Region 10 Conf. (TENCON), pp. 1182-1186, 2020.